JACS
JOURNAL OF THE AMERICAN CHEMICAL SOCIETY

Article

pubs.acs.org/JACS

Edgeless Ag–Pt Bimetallic Nanocages: In Situ Monitor Plasmon-Induced Suppression of Hydrogen Peroxide Formation

Sheng-Chih Lin, Chia-Shuo Hsu, Shih-Yun Chiu, Tzu-Yu Liao, and Hao Ming Chen*

Department of Chemistry, National Taiwan University, Taipei 106, Taiwan

Supporting Information

ABSTRACT: Improvements in the performance of electrocatalysts, along with continuing advances in selective pathway for target reaction, have great potential to offer opportunities in designing competitive reactions especially for using a photophysical process owing to its tunable properties. Herein, we demonstrated a first empirical evidence of suppressing the formation of undesired peroxide intermediate through plasmonic effects, in which plasmonic Ag–Pt bimetallic nanocages were synthesized with an edgeless feature, and a custom-made RDE/RRDE working station was designed to provide unique means by which to in situ realize the plasmon-induced effects toward the target reaction. The edgeless Ag–Pt bimetallic nanocages with hollow interior performed newly plasmon-induced effects, which was characteristic of photodependent nature to suppress the formation of undesired peroxide intermediate. We concluded that the plasmon-induced hot electron transfer governed the suppression of peroxide formation instead of plasmon-induced heating that would cause a negative effect (i.e., increase of peroxide yield), in which the hot electron transfer of Ag nanostructure offered a sufficient energy to populate the antibonding orbital of O_2 as illustrated by in situ X-ray absorption approach. This rapid light-dependent nature corresponding to localized surface plasmon resonance in present nanocages can potentially offer synergetic strategies toward altering the chemical reactions or reaction pathways in various fields.

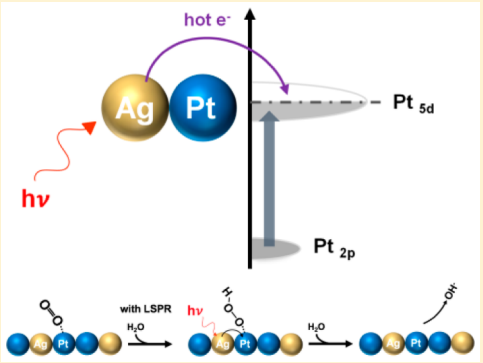

INTRODUCTION

Oxygen reduction reaction in alkaline electrolyte is a critical reaction for developing electrochemical systems relative to energy conversion especially for metal-air battery and fuel cell that offer alternative opportunities to utilize cleaner and greener energy sources without undesired exhaust. To date, platinum-based electrocatalysts have exhibited the highest performance in catalyzing oxygen reduction,[1] yet employment of Pt is undesired owing to its expensive cost. With the aim of substituting for Pt, numerous studies of multimetallic nanostructures such as NiPt,[2,3] PtPd,[4] AgCo,[5] AuCuPt[6] and AgCuPd[7] have been demonstrated to perform comparable activities in catalyzing oxygen reduction. The activity and mechanism of oxygen reduction reaction are strongly dependent on the intrinsic surface nature of electrocatalysts that directly related to the element and crystalline facets of electrocatalysts.[1] For example, the ORR activity of platinum nanoparticles decreased in a series of hexagonal > cubic > spherical > tetrahedral nanostructures in acidic electrolyte.[8] Besides, another crucial factor, formation of hydrogen peroxide intermediate, needs to be taken into account when considering a perfect catalyst toward oxygen reduction. Regarding this issue, the oxygen reduction reaction commonly involves a four-electron transfer to produce water, whereas another parallel reaction that involves a two-electron transferring pathway with producing an undesired intermediate simultaneously competes against the initial four-electron transfer. This intermediate, hydrogen peroxide (H_2O_2), further occurs undesired side-reactions and probably leads to a loss in overall efficiency. Consequently, any improvements in the performance of electrocatalysts, along with continuing advances in suppressing the undesired intermediate, have great potential to offer opportunities in designing competitive reactions especially for using a photophysical process owing to its tunable properties.

The localized surface plasmon resonance (LSPR) is an inherent oscillation of free-like electrons on the surface of metal material excited by incident irradiation, which leads to an optically enhanced absorption and scattering on nanostructures, especially for copper, silver and gold. The plasmonics researches have rapidly expanded owing to their easily tailoring and shape-dependent optical nature,[9−12] these specific natures result in wide applications of LSPR in various fields.[1,13−23] In the LSPR process, the collective excitation of the free electron on metallic nanostructure, known as surface plasmons, is occurred first, after that the surface plasmons decay through radiative emission of photons or nonradiative excitation of electrons in a solid, leading to two types of carriers including a hole and an electron. These carriers are considered "hot" since their energies are larger than those of thermal excitations at ambient temperature.[24] Recently, it was observed that hot carriers generated by nonradiative decay facilitated some

Received: August 30, 2016
Published: January 27, 2017

DOI: 10.1021/jacs.6b09080
J. Am. Chem. Soc. 2017, 139, 2224–2233

chemical reactions.[25,26] For instant, gold and silver nanostructures were able to active $^3O_2$ or achieve room temperature hydrogen dissociation by employing LSPR to inject electrons.[27,28] The plasmonic heating could be employed to grow nanostructure[29] or achieve photothermal therapy of tumor cell.[30] Consequently, the plasmon-induced effects have been revealed to provide great potentials in various fields that taken the advantage of plasmonic nanostructures to amplify their specific propeties.

In this study, we reported a first empirical evidence of suppressing the peroxide intermediate through plasmonic effects from LSPR. A customized electrochemical measurement station was developed here to achieve an in situ monitor of plasmon-induced effects upon suppression of peroxide intermediate. Furthermore, plasmonic edgeless bimetallic nanocages were synthesized as a model system with a desired elemental combination of Ag and Pt, because Pt had been well explored and could offer excellent activity while the Ag was able to generate LSPR effects. Note that silver was employed as model system instead of gold, since the silver thermodynamically favored forming alloy with platinum ions through galvanic replacement. Additionally, a selectively control of chemical reaction through plasmonic effects strongly relies on precisely manipulating the interactions between plasmonic metal and reactants, the significant contact between plasmonic element (Ag) and reactive element (Pt) that acts as major reactive site can boost the plasmon-induced effects onto the peroxide formation.

EXPERIMENTAL SECTION

Chemicals. Silver nitrate (99.9999%) and poly(vinylpyrrolidone) (PVP; M_w = 55 000) were purchased from Sigma-Aldrich, cupric chloride (98%) was purchased from Fisher Scientific. 1,5-petanediol (98%) and hydrogen hexachloroplatinate (IV) hydrate (99.9%) were purchased from ACROS.

Ag Nanocubes Synthesis. Ag nanocubes were prepared using a polyol reduction of silver ions. Metal salts solution which contained silver nitrate (120 mM) and cupric chloride (0.38 mM) was prepared first by dissolving in 1,5-petanediol (10.0 mL). Capping agent solution was prepared by dissolving 0.20 g of poly(vinylpyrrolidone) into 10.0 mL of 1,5-petanediol. Another 1,5-pentanediol (20.0 mL) was heated to 190 °C and stirred for 10 min as stock solution. Both metal salt solution (5 mL) and capping agent solution (5 mL) were simultaneously injected the preheated stock solution (1,5-pentanediol) with a desired injection rate of 500 μL/min. All reactions were operated in silicone oil bath with temperature-controlled unit.

Ag−Pt Bimetallic Nanocages Synthesis. 160 μL of Ag nanocubes (~80 nm in edge length) was added to 5 mL deionized water and then refluxed for 8 min. Desired volume of $PtCl_6^{2-}$ solution (1 mM) was slowly dropped into a diluted Ag nanocubes solution and refluxed for another 10 min to achieve uniformly reacting, the resulting products were obtained after cooling to room temperature. Various volumes including 15, 30, 45, and 60 μL of $PtCl_6^{2-}$ solution were used for each sample, as named AgPt-15, AgPt-30, AgPt-45, and AgPt-60 in present study, respectively. After reacting with $PtCl_6^{2-}$ ions, residual AgCl precipitate was dissolved by adding NaCl salt until getting a saturated solution of NaCl. To remove the residual species, the resulting solution was centrifuged at 12 000 rpm for 15 min and rinsed with water. This process was repeated several times to get rid of NaCl, finally the samples were dispersed in water before further analysis.

Structural Characterization. The UV−visible spectra were collected using JASCO V-670 spectrophotometer, and scanning electron microscopy (SEM) images were obtained with JSM-6700F (JEOL). Transmission electron microscopy (TEM) images were conducted by Hitachi H-7650 operated at 100 kV, and High-resolution-TEM images were performed at JEOL JEM-2100F operated at 200 kV with equipping energy-dispersive X-ray (EDX) spectrometer.

Electrochemical Characterization. All measurements were carried out by using rotating disk electrode (RDE) voltammetry upon a glassy carbon (GC) disk at 1600 rpm, in which rotating disk working electrode made of glassy carbon (GC electrode, 5 mm in diameter, PINE:AFE3T050GC PINE, area: 0.196 cm^2) connected to a CHI-704E bipotentiostat (CHI Instruments). In the case of rotating ring disk electrode (RRDE), The RRDE experiments were performed with E7R9 series electrode including a 0.2475 cm^2 disk and a 0.1866 cm^2 ring with collection efficiency of 0.37. The electrochemical experiments were proceeding at 25 °C in either N_2- or O_2-saturated 0.1 M KOH using a standard three-electrode electrochemical setup. The working electrode was RDE or RRDE, while the counter electrode and reference electrode was platinum grid and Ag/AgCl (0.21 V vs NHE) electrode, respectively. A custom-made RDE/RRDE station designed with the aim of realizing the plasmonic effects, where the irradiation from xenon lamp with an intensity of 200 mW/cm^2 was employed and light response was measured in either 5 or 10 s interval between light on and off. 100 μL of sample solution with a fixed concentration (21.4 mg/mL) was first mixed with 1 mg carbon black to achieve better dispersion, then 20 μL of above mixture solution was loaded on either RDE or RRDE as working electrode. After drying in room temperature, 20 μL of 10% Nafion/isopropanol solution was dropped upon electrode surface to protect electrocatalysts from peeling off. The cyclic voltammograms of all samples carried out in 0.1 M KOH prepurged N_2 for 1 h, and then the solution was purged O_2 for another hour to make sure O_2-saturated for linear sweep voltammetry (LSV) measurements and 5 s intervals were set to light response detection. The fraction of peroxide (HO_2^-) formation could be demonstrated by the relation between ring current and disk current. The fraction of peroxide ($X_{peroxide}$) is calculated by eq 1:

$$X_{peroxide} = \frac{\frac{2I_R}{N}}{I_D + \frac{I_R}{N}} \quad (1)$$

where I_R is the ring current, I_D is the disk current, and N is the collection efficiency. In order to realize the LSPR effects carrying out in the limiting current region, we chose amperometric $i-t$ curve mode and set fixed potentials of 0.5 V (vs RHE) on disk electrode and 1.4 V (vs RHE) on Pt ring electrode. Furthermore, fraction of peroxide change (FPC) was employed herein to evaluate the light-induced peroxide yield change and was defined as eq 2:

$$\text{fraction of peroxide change (FPC)} = \frac{\Delta X}{X_{dark}} = \frac{X_{light} - X_{dark}}{X_{dark}} \quad (2)$$

In Situ X-ray Absorption Spectroscopy and Powder Diffraction Spectroscopy. All Ag−Pt nanocages were dried to obtain powder form, and packed in 3 M scotch tapes for X-ray absorption measurements, in which the measurement of each sample were carried out for twice, light off and light on. The light source was the same as mentioned in Electrochemical Characterization section. Pt L_3-edge X-ray absorption spectra were recorded from 11 363 to 11 861 eV (energy of Pt L_3-edge is 11 564 eV) at beamline BL01C1 at the National Synchrotron Radiation Research Center (NSRRC) in Taiwan, the electron storage ring was operated at 1.5 GeV with a constant current of 360 mA. The relative vacancy values were calculated the integration area under the in situ XAS curves between 11 567 eV and 11 584 eV. Powder X-ray diffraction data were collected on beamline 09A at the Taiwan Photon Source (TPS) of the National Synchrotron Radiation Research Center. The 15 keV X-ray source is delivered from an in-vacuum undulator (IU22). The powder diffraction patterns were recorded by a position-sensitive detector, MYTHEN 24K, covering a 2θ range of 120°. The detector is mounted on the concentric large three-circle diffractometer. Powder sample was loaded into a 0.2 mm capillary for uniform absorption and faster rotation during data collection. Because of the small gaps between

DOI: 10.1021/jacs.6b09080
J. Am. Chem. Soc. 2017, 139, 2224−2233

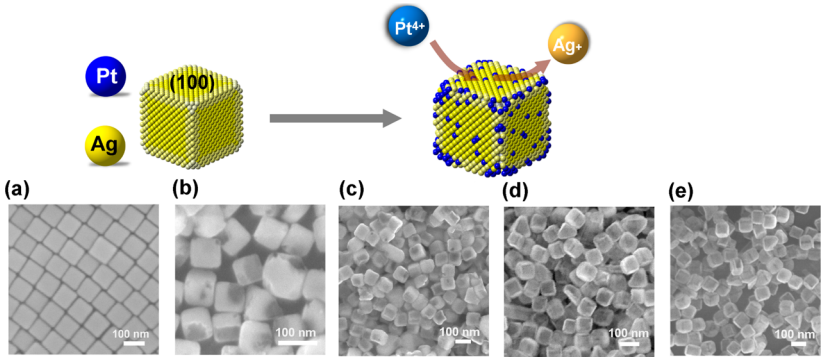

Figure 1. SEM images of (a) Ag nanocubes, (b) AgPt-15 μL, (c) AgPt-30 μL, (d) AgPt-45 μL, and (e) AgPt-60 μL samples; upper part shows the schematic diagram of galvanic replacement between Ag^0 and Pt^{4+}.

detector modules, two data sets were collected 2° apart and the data were merged to give a continuous data set.

RESULTS AND DISCUSSION

Structural Characterization. Ag nanocubes were synthesized through a modified polyol process similar to previous reports,[31,32] which allowed us employing the Ag nanostructure as sacrificial template to fabricate the desired Ag−Pt bimetallic nanostructures by utilizing galvanic replacement reaction.[33] Scanning electron microscope (SEM) images of Ag nanocubes before/after reacting with various amounts of K_2PtCl_6 solution (1 mM) at 100 °C were shown in Figure 1. The Ag nanocubes were characteristic of smooth surface and a mean edge size approximately 81 nm with a standard deviation of 7 nm (Figure 1a, suggesting the Ag nanocube with well-control shape and facet (exposed {100} facet to electrolyte) could eliminate the contribution caused by facets and shape/size. Once a small amount of $PtCl_6^{2-}$ solution (15 μL) was introduced into Ag nanocubes solution, the formation of small hole on Ag nanocube (Figure 1b; AgPt-15 μL) indicated that replacement reaction between Ag^0 and Pt^{4+} was evidently occurred. With further increasing the amount of $PtCl_6^{2-}$ solution, the surface of resulting Ag−Pt bimetallic nanostructure considerably became rough (Figures 1c and 1d; AgPt-30 μL and AgPt-45 μL) and finally the Ag−Pt bimetallic nanocages were fabricated (Figure 1e; AgPt-60 μL). Besides, UV−vis spectra of the Ag nanocubes after reacting with various amounts of $PtCl_6^{2-}$ solution verified that the pristine Ag nanocubes exhibited a LSPR major peak at ~510 nm with three small shoulder peaks at 452 nm, 391 nm, 345 nm (Figure 2). Once a 15 μL of $PtCl_6^{2-}$ solution was added into the reaction system, the major LSPR peak of nanocubes red-shifted from 510 to 526 nm with slightly broadening. Note that those three shoulder peaks became undistinguishable, indicated that the LSPR nature of the pristine Ag nanocubes was distorted by forming Pt atoms onto the surface of Ag cubes. Accompanying with the formation of Pt on the surface, the LSPR properties of Ag nanocubes with a sharp extinction peak disappeared and became a broaden peak at longer wavelength region. Progressive covering of Pt would result in a significant red-shift from 526 nm (AgPt-15 μL) to 645 nm (AgPt-60 μL), this observation was consistent with the cases of replacement for both Au[34] and Pd[35] cases upon Ag nanocubes. To further verify the deposition of Pt over Ag nanocubes, elemental ICP-MASS analysis was conducted to confirm both the Pt and Ag contents in present bimetallic system. Pt content considerably raised from 4.4% (AgPt-15 μL) to 23.2% (AgPt-60 μL) with increasing the $PtCl_6^{2-}$ amount

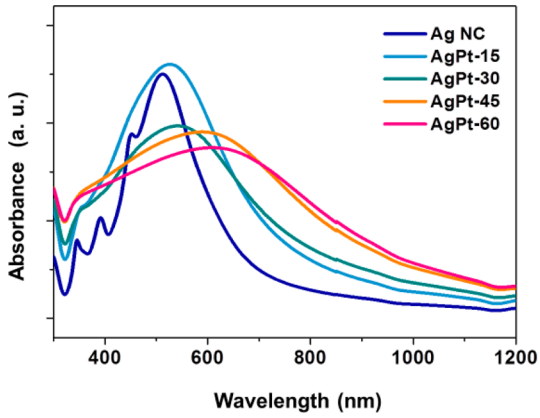

Figure 2. UV−vis spectra of Ag, AgPt-15 μL, AgPt-30 μL, AgPt-45 μL, and AgPt-60 μL samples.

(Table 1), implied that the Pt amount deposited on the Ag nanocubes could be controlled by varying the volume of $PtCl_6^{2-}$ solution.

Table 1. Elemental ICP-MASS Analysis of Ag, AgPt-15 μL, AgPt-30 μL, AgPt-45 μL, and AgPt-60 μL Samples Represented in Atomic %

sample	Ag content (%)	Pt content (%)
Ag	100.0	–
AgPt-15 μL	95.54	4.46
AgPt-30 μL	93.78	6.22
AgPt-45 μL	86.98	13.02
AgPt-60 μL	76.78	23.22

Most specifically, the holes were clearly observed at the corner/edge of nanocube rather than the {100} faces of cube, elucidated that this replacement was locally initiated at corner or edge instead of face. To resolve this galvanic replacement between Ag nanocubes and Pt^{4+} ions, transmission electron microscope (TEM) images with increasing the $PtCl_6^{2-}$ amount were displayed in Figure 3a. Note that the galvanic replacement launched at corner or edge, which differed from the observation in Ag−Au replacement that clarified galvanic replacement of (100) facet on Ag nanocubes.[33] It was worth saying that the replacement would start from the site with relatively high surface energy, the surface free energies of low-index facets decreased in an order of (110) > (100) > (111) facet. In present system, the selective capping of (100) facet of Ag

DOI: 10.1021/jacs.6b09080
J. Am. Chem. Soc. 2017, 139, 2224−2233

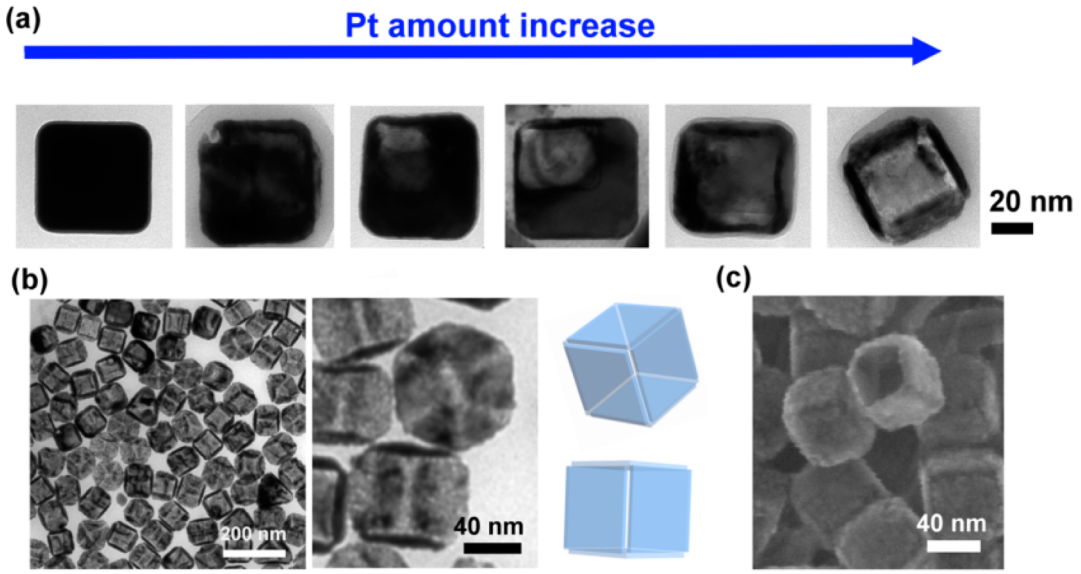

Figure 3. (a) TEM images of structural evolution of single nanocube during galvanic replacement with increasing Pt amount. (b) Different perspectives of edgeless Ag−Pt nanocages along [111] and [110] zone axes and the corresponding geometrical models. (c) SEM image of crashed Ag−Pt nanocages.

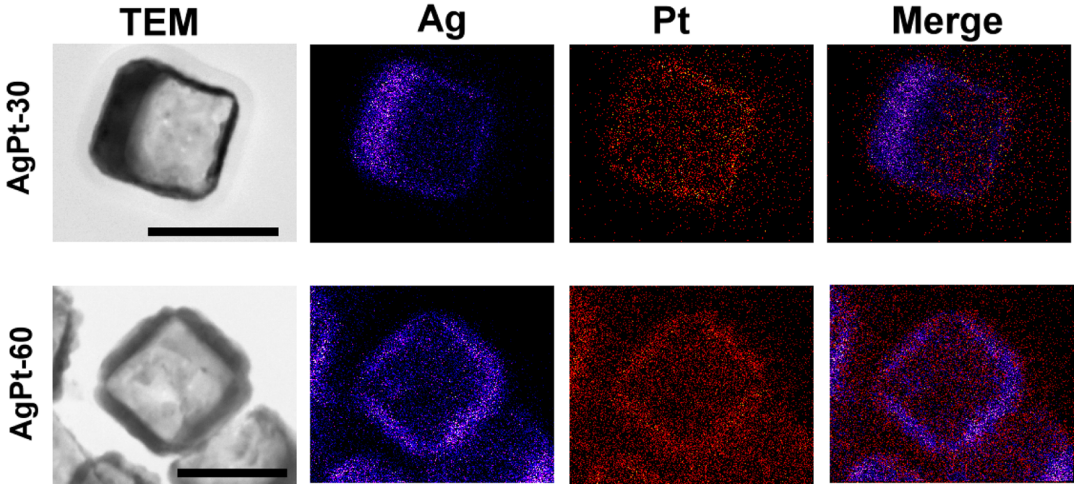

Figure 4. TEM images and corresponding element mappings of AgPt-30 and AgPt-60 samples. Scale bar is 80 nm.

nanocube by PVP, the capping polymer, could lead to a decrease of surface free energy in (100) facet,[35] which gave rise to an energetic order of (110) > (111) > (100) in the presence of PVP. Consequently, the replacement reaction would remarkably initiate on the reactive sites of (110)/(111) facets, thereby leading to the dissolution of silver and further generating of hole on edge ({110} facets) or corner ({111} facets) of cube. Ag oxidation in galvanic reaction would release electrons and result in reduction of Pt^{4+} ions, while the elemental Pt generated by replacement would be self-catalytically deposited on the surface of nanocube owing to a good matching of crystal structure (both Ag and Pt are crystallized in face-centered cubic). Notably, the newly generated Pt atoms would grow upon {100} facets rather than {110}/{111} facets (edge/corner), which led to Ag−Pt bimetallic nanostructures with the absence of edge/corner (edgeless nanocages). Numerous perspectives of Ag−Pt nanocages were observed in TEM image from different orientations, as shown in Figure 3b, two typical orientations were identified as projections aligned with the [111] and [110] zone axes of the edgeless nanocages. Brighter parts of nanocage in projected TEM image were clearly observed, revealed the formation of an edgeless feature consisting of unique architecture with crystallographically independent faces. Remarkably, the crashed Ag−Pt nanostructure as illustrated in Figure 3c was characterized by coreless with hollow interior. Therefore, these images provided unequivocal evidence for the selective growth of Pt on the {100} facet of the nanocube and implicated bimetallic edgeless nanocage was robust to maintain its three-dimensional structure, which allow providing additional channels to reactants as compared with nanobox counterpart.

Note that a situation of the formation of individual Ag and Pt nanostructures could be ruled out here, since the X-ray diffraction patterns of all samples via synchrotron radiation light source were characteristic of bimetallic nature rather than the individually forming Ag or Pt nanostructure (without significantly contacting in between), in which the XRD patterns of all samples confirmed that all bimetallic nanostructures crystallized with Face-centered cubic structure (as shown in

DOI: 10.1021/jacs.6b09080
J. Am. Chem. Soc. 2017, 139, 2224−2233

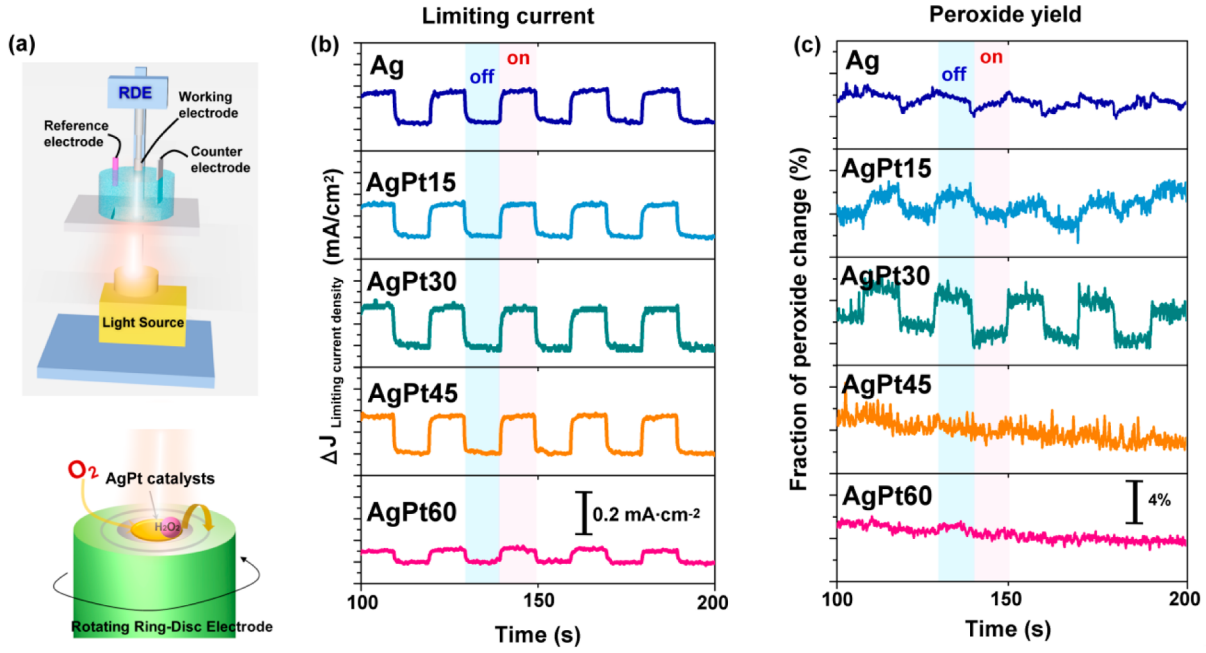

Figure 5. (a) Schematic diagram of experimental setup and working concept in RRDE. Difference of limiting current density (b) and fraction of peroxide change (c) under chopped light for various samples.

Figure S1) with absence of remarkable byproducts or unexpected phases. Furthermore, considerable shifts toward higher diffraction angle were confirmed with increasing the amount of Pt, which could be attributed to the relatively smaller atomic radius of Pt atoms and implied the formation of bimetallic nanostructures. On the other hand, the elemental distributions of individual nanostructures conducted through TEM-EDX were shown in Figure 4 and S2, where the corresponding elementally mapping of Ag and Pt were found on the position of the nanostructures. It could be obtained from element map that the element of both Ag and Pt existed in the nanostructures. Notably, a clearly thin shell made of both Ag and Pt could be evidently revealed in AgPt-15 (Figure S2) and AgPt-30 (Figure 4) samples, indicating that bimetallic Ag–Pt nanoshell was formed at early stage while unreacted Ag cube was confirmed by the presence of element Ag in the center of cube. With increasing the Pt amount, the unreacted Ag core disappeared while the thickness of bimetallic Ag–Pt increased. Notably, as shown in Figure 4 (AgPt-60), more elemental Pt was obtained in the outermost surface of bimetallic AgPt nanocages once most Ag core was depleted with a nanocage feature. Consequently, these images provided clearly evidence for the formation of bimetallic Ag–Pt nanosehll, and also elucidated that more Pt atoms presented onto the outermost surface once sequent Pt atoms were generated by replacement reaction.

In Situ Monitor of Light-Induced Effects upon Peroxide Yield. It was noteworthy to say that the real-time monitor of the change of peroxide yield could not be achieved through conventional approaches. A custom-made RDE/RRDE station was needed and designed with the aim of realizing the plasmonic effects toward the target reaction as illustrated in Figure 5a and Figure S3 (corresponding photographs), where the RRDE was employed to investigate the formation of peroxide intermediate and allowed us revealing the formation of hydrogen peroxide in real-time for obtaining the plasmon-induced effects upon the reactions. Because our goal was to monitor the plasmon-induced phenomenon with the absence of kinetics influences, the amperometric i–t mode was carried out with a fixed potential of 0.5 V (vs RHE) corresponding to the mass-transfer limited condition with the aim of eliminating the contributions from reaction kinetics which strongly depended on the intrinsic nature of materials. As shown in Figure 5b, in the steady-state mass-transfer-limited region, there were unprecedented current enhancements for all Ag–Pt edgeless nanocages samples. The enhanced current densities (ΔJ) of various samples were similar (approximately 0.15 mA/cm^2) except AgPt-60 μL sample (0.05 mA/cm^2), suggested that this enhancement possibly resulted from the plasmonic effects of Ag since this light-induced enhancement in limiting current was likely characteristic of Ag amount-dependent nature. The noteworthy feature was the onset potentials and corresponding $E_{1/2}$ values that shifted to higher potential region in dark condition with increasing Pt amount (Figure S4), which could be ascribed to the existence of Pt on the surface while Ag nanocubes only exhibited a lowest performance in catalyzing oxygen reduction. This phenomenon concluded that the presence of more Pt atoms onto the outermost surface of bimetallic edgeless nanocages could lead to higher onset potentials and corresponding $E_{1/2}$ values because of higher intrinsic activity of Pt element,[1] this result corresponded to the observations from structural studies that revealed the presence of Pt onto the outermost surface (Figure 4).

It was evidently that, in addition to enhancement in limiting current density, the light illumination upon bimetallic AgPt nanocages was able to produce a phenomenon for suppressing the formation of peroxide (Figure 5c). The fraction of peroxide change was employed herein to evaluate the light-induced change of peroxide (as defined in Experimental Section). Most interestingly, the fraction of peroxide change as a function of time in Ag, AgPt-15 μL, and AgPt-30 μL samples exhibited a rapid response to the light illumination, and cohered with the enhanced current density (Figure 5c), this phenomenon clearly revealed that the light-induced effects were able to suppress the

DOI: 10.1021/jacs.6b09080
J. Am. Chem. Soc. 2017, 139, 2224–2233

formation of peroxide. To the best of our knowledge, this is the first demonstration that light-induced effects can reveal a rapidly coherent nature in enhancing current density and suppressing peroxide yield. It was worth noting that this tunable suppression of peroxide yield was solely occurred in the samples of Ag, AgPt-15 μL and AgPt-30 μL, whereas both AgPt-45 μL and AgPt-60 μL samples failed to perform this specific phenomenon.

In order to further clarify the reasons behind these light-induced phenomena, a control measurement for a commercial Pt/C sample was conducted in the identical condition while the amperometric i–t mode was carried out to obtain the light-induced effects upon limiting current. As illustrated in Figure 6,

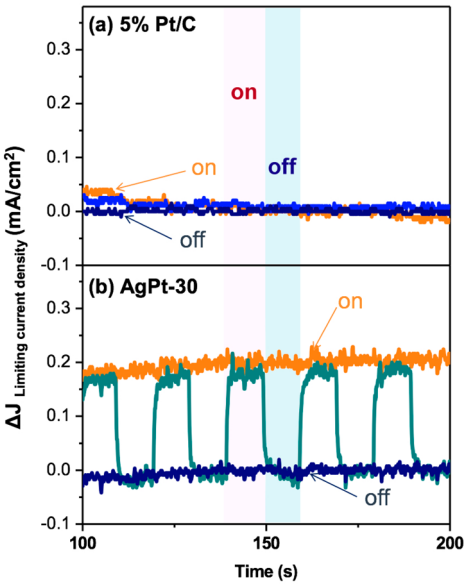

Figure 6. Difference of limiting current density for commercial Pt/C sample (a) and AgPt-30 sample (b) under chopped light.

the light illumination failed to generate any remarkable effect upon commercial Pt/C sample (Figure 6a and Figure S5), whereas an evidently coherent nature with illuminating of on/off cycle in enhancing limiting current was present in AgPt-30 μL sample (Figure 6b). To further consider the diffusion-limited current (I_d) that can be expressed as eq 3:[36]

$$I_d = 0.62 n_e F A C_{O_2} D_{O_2}^{2/3} \upsilon^{-1/6} \omega^{1/2} \quad (3)$$

where n_e is the number of overall electron transfer in oxygen reduction, F is Faraday constant (F = 96 485 C/mol), C_{O_2} is the bulk concentration of O_2 (1.2×10^{-3} M), D_{O_2} is the diffusion coefficient of O_2 in aqueous solution (1.9×10^{-5} cm^2/s), ν is the kinetic viscosity of electrolyte (0.01 cm^2/s) and ω is the rotating speed.[37,38] Apparently the current is proportion to $D^{2/3}$ (diffusion coefficient) of reactant that is strongly dependent on the temperature.[39] For this reason, it could be easily expected that the light illumination might give rise to increasing the temperature of electrolyte and further enhance the mass-transfer, which would lead to the enhancement in limiting current. That is, an experiment of temperature effects was performed to ascertain the light-induced influences on both limiting current density and the change of peroxide formation. As illustrated in Figure 7, the limiting current density and the fraction of peroxide change were plotted as a function of

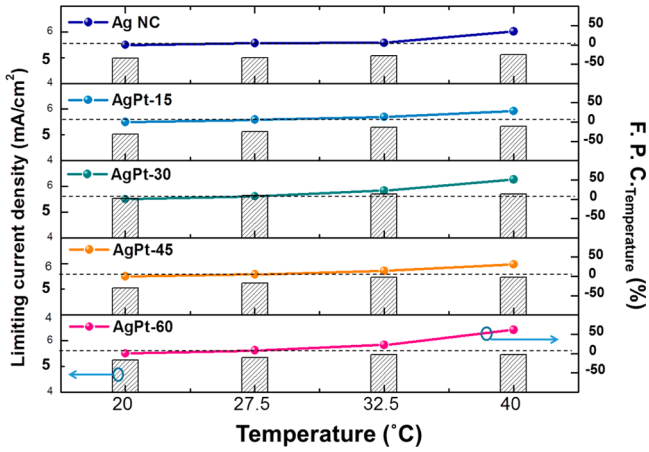

Figure 7. Limiting current densities and fraction of peroxide changes as a function of temperature for various samples.

temperature, in which the limiting current densities of all samples were characteristic of an increase trend with raising the temperature. Because the raise of temperature could facilitate the migration of reactant and further promote the catalysis, and the limiting current would be enhanced by increasing the temperature. In present measurement, the diffusion coefficient of O_2 in water increased by approximately 54% from 20 °C (1.80×10^{-5} cm^2/s) to 40 °C (2.78×10^{-5} cm^2/s),[39] thereby leading to an increase in limiting current that was determined by diffusion limitation of reactant. In this case, the resulting limiting current densities of all samples with increasing the temperature exhibited enhancement by approximately 3–8%.

Most interestingly, the fraction of peroxide formation increased with temperature even though the limiting current increased, a behavior that opposite to the features of light illumination we had obtained above (Figure 7), indicated that the peroxide yield considerably increased with raising the system temperature. Consequently, this facilitation in reactant diffusion by increasing temperature seems to cause a positive effect on enhancement of limiting current but accompany a negative effect on peroxide yield (i.e., facilitating the peroxide formation). The system temperature in present study, however, was well controlled in a constant temperature (~25 °C) by a thermostatic water bath, meant that explicit temperature variation was absent even though the heating as a result of illuminating could lead to an increase of temperature. Furthermore, it was evident that temperature raising would result in a contrary effect to our observation that the suppression of peroxide yield was clearly revealed. On the basis of the above-mentioned results, we could unambiguously conclude that the light-induced heating generated conflicting effort to boost the formation of peroxide yield and could be ruled out for contributing significant effects in suppressing the peroxide formation. Accordingly, we suggested that these light-induced effects might be attributed to the LSPR effects from Ag–Pt bimetallic nanomaterials.

Note that both AgPt-45 and AgPt-60 samples exhibited the smallest light-induced features in limiting current among all samples while the curve of peroxide change lacked of any photoresponse, suggested that present light-induced phenomenon might be attributed to the LSPR effects from Ag, since the most surface of AgPt-60 sample was covered by plasmonic effects-free element of Pt (as shown in Figure 4). With this in mind, two monochromatic irradiations of 532 and 1064 nm

DOI: 10.1021/jacs.6b09080
J. Am. Chem. Soc. 2017, 139, 2224–2233

were employed to further investigate these light-induced effects due to a wavelength-dependent nature of plasmon-induced effects.[11] The limiting current densities and fractions of peroxide change under chopped monochromatic irradiations as illustrated in Figure 8 clearly clarified different behaviors in

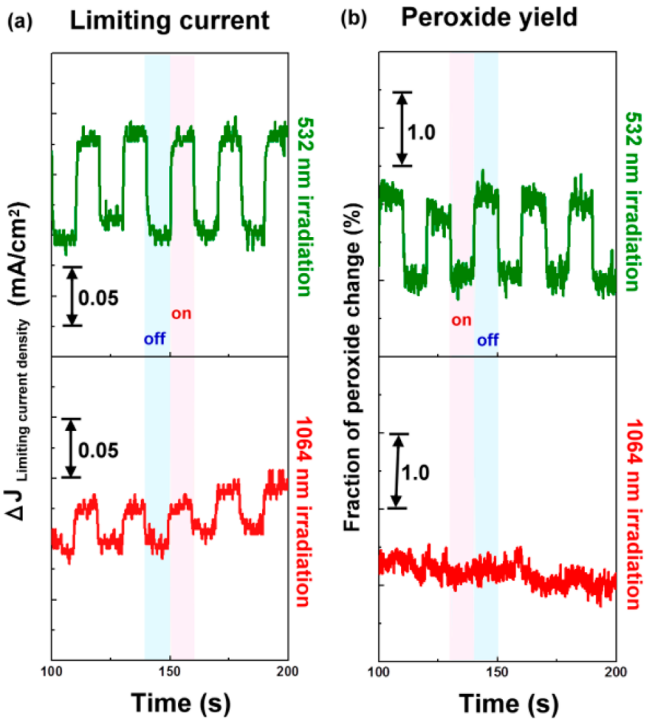

Figure 8. Difference of limiting current density (a) and fraction of peroxide change (b) for AgPt-30 sample under chopped monochromatic irradiations of 532 and 1064 nm.

532 and 1064 nm irradiations. Both irradiations of 532 and 1064 nm could perform increase in limiting current, whereas only irradiation of 532 nm could significantly suppress the formation of peroxide while the peroxide yield under chopped irradiation of 1064 nm remained steady. This empirical evidence further supported our suggestion that these light-induced effects resulted from the LSPR of Ag, since present AgPt nanocages exhibited a strong LSPR absorption at 532 nm with absence of significant plasmon resonance at the region of 1064 nm (Figure 2).

Although these AgPt edgeless nanocages were characteristic of porous nature as illustrated in Figure 3, this bimetallic nanocages could exhibit a long-term stability in alkaline electrolyte over a period of 2000 cycles, maintaining 98.8% of its initial current density (Figure 9). Present plasmon-induced effects could perform a similar phenomenon and work in acidic

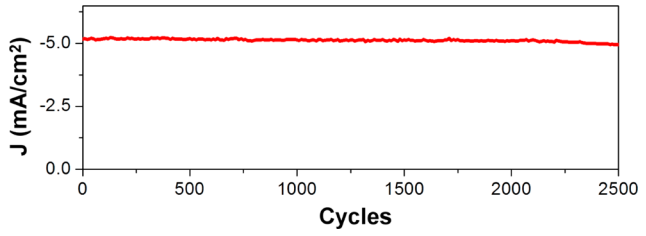

Figure 9. Limiting current density as a function of cycle numbers under a fixed potential of 0.5 V (vs RHE) for AgPt-30 sample.

electrolyte as well. Nevertheless, the limiting current declined rapidly within several minutes since the Ag atoms could not survive in acidic condition. As a consequence, the correlation can be probably characterized by a positive relationship between LSPR effects and suppression of peroxide yield, in contrast to limiting current that was typically improved by numerous factors such as lattice strain of and/or corresponding *d*-band status of multimetallic nanoalloy.[40−43] For this reason, we aim to ascertain a direct correlation between LSPR induced-effects and the change of peroxide yield, that should be more imperative for future applications of LSPR.

Plasmon-Induced Effects Studies. Although above-mentioned light-induced phenomena could be attributed to the LSPR effects with the wavelength-dependent nature, yet they also indicated that the enhancement in limiting current and suppression of peroxide formation were caused by various factors which might be generated by LSPR. In this case, to ascertain the detail mechanism behind this tunable nature, three plasmon-induced effects including heating, generation of electromagnetic field, and charge transfer of hot electrons have to be simultaneously considered.[24,25] Note that a situation that observed plasmon-induced effects were attributed to the contributions from individual Ag and Pt nanostructures could be ruled out here, since the X-ray diffraction patterns of all samples were characteristic of bimetallic nature rather than the individually forming Ag or Pt nanostructure (as shown in Figure S1).

First, the plamon-induced local heating that involved an internal decay of hot carriers inside metallic nanoparticles could be considered, in which the localized heating gave rise to a temperature raise in both the nanostructure itself and its immediate environment.[24,44] According to the observations in Figure 7, the plasmon-induced heating could be excluded from contributing the suppression of peroxide formation because of the conflicting change in peroxide formation. However, we believe that the increase of limiting current could be attributed to the plasmon-induced heating instead of illumination-induced heating, since the electrolyte temperature in present study was controlled (~25 °C) well with absence of large perturbation in temperature. Additionally, the enhancement of limiting current was characteristic of the coherent nature and rapid response with chopped illumination, which also further elucidated the dominance from plasmon-induced heating.

Regarding aforementioned plasmon-induced heating that might fail to greatly suppress the peroxide yield, another plasmon-induced effect (i.e., transfer of hot electrons) might play vital roles to suppress the peroxide yield. Because the nature of oxygen reduction remarkably relied on the *d*-band structure of metallic nanomaterials, the plasmon-induced effects might modify the *d*-band character of Pt and further determine its activity. Toward this end, X-ray absorption spectroscopy was employed to offer meaningful indication of the *d*-band character of absorbing atoms,[22,45] in which in situ measurement was conducted to reveal the light illumination effects (Figure 10a and S6). To offer further insight for elucidating the affects from LSPR upon the interaction, the X-ray absorption near edge structure (XANES) of the Pt L_3-edge was utilized to realize these phenomena. Since we suggested Pt atoms still acted as active sites and the L_3-edge absorption involved the transition from *2p* to *5d* states while the band character of Pt comprised mainly Pt_{5d} states, meant that a lower intensity in XANES indicated the presence of less vacancies upon *5d* state. As displayed in Figure 10b, once the plasmon-induced hot electron

DOI: 10.1021/jacs.6b09080
J. Am. Chem. Soc. 2017, 139, 2224−2233

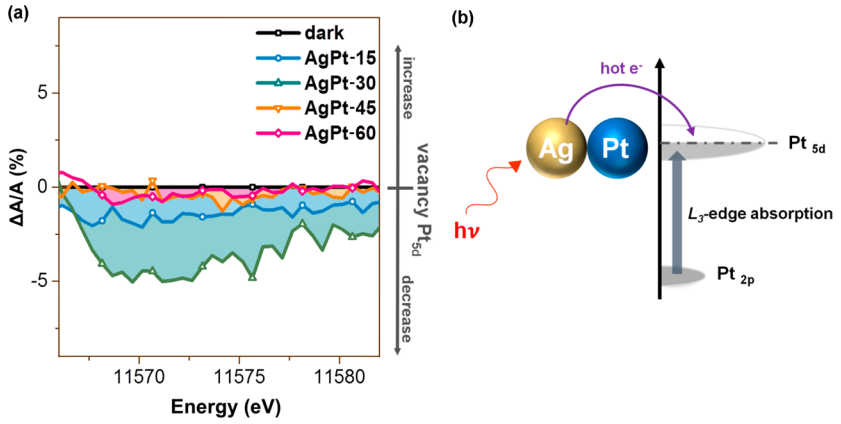

Figure 10. (a) Relative vacancy upon Pt_{5d} states for various samples under light illumination. (b) Schematic diagram of Pt L_3-edge XANES and hot electron transfer.

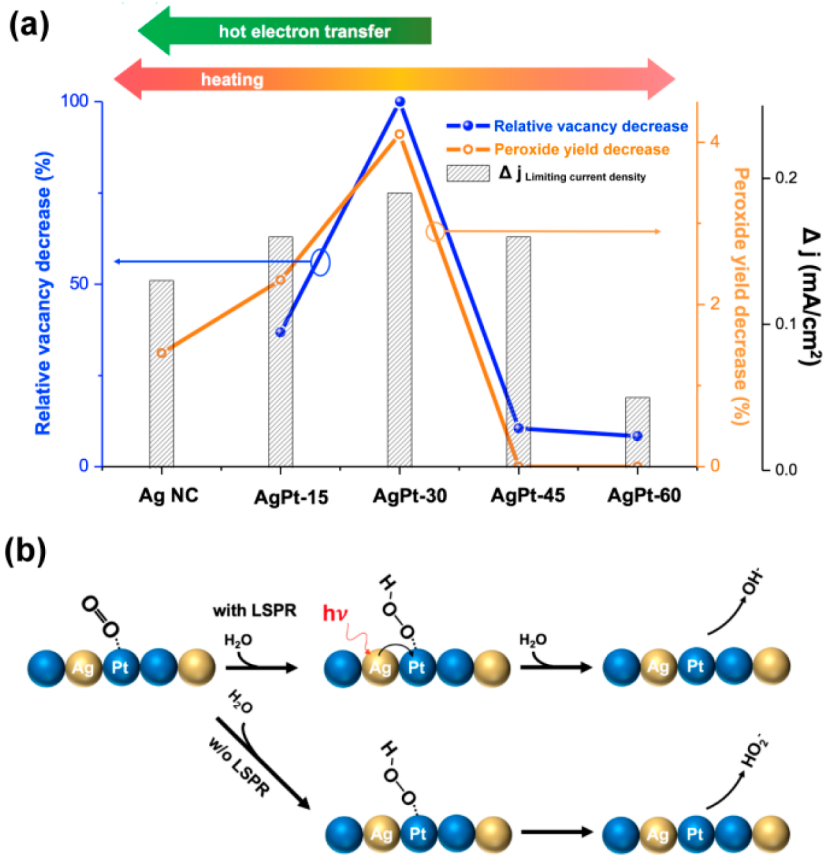

Figure 11. (a) Experimental comparison of the limiting current density, peroxide yield decrease, and the relative vacancy decrease among various samples. (b) Schematic diagram of mechanism in suppressing peroxide yield through hot electron transfer.

transfer occurred, the electron density upon Pt *d*-band character would decrease and thereby leading to a decline in absorbance of Pt L_3-edge XANES, the difference between the XANES of various samples in dark and that of the illuminated situations obtained the relative vacancy ($\Delta A/A$) on Pt. With the presence of light illumination, it was unambiguous that a decrease in relative vacancy as a result of hot electron transfer was evident for all samples, indicated that in situ Pt L_3-edge of XANES provided an appropriate account for this plasmonic hot electron transfer from Ag to Pt. This result demonstrated that the AgPt-30 sample revealed the largest decrease in relative vacancy and gave rise to a decrease order of AgPt-30 > AgPt-15 > AgPt-45 > AgPt-60 under illumination.

On the other hand, it could be expected that plasmon-induced electromagnetic field were able to facilitate the rapid migration of reactants/products nearby the Ag−Pt nanocages. Notably, since the onset potential values of various samples corresponded to the Pt amount onto the surface (Figure S4), suggested a fact that Pt atoms still acted as active sites rather than Ag atoms. Once the Pt amount was increased further and covered the outermost surface of Ag−Pt bimetallic nanocages, plasmon-induced enhancement of limiting current density revealed a significant decline and almost disappeared (Figure

DOI: 10.1021/jacs.6b09080
J. Am. Chem. Soc. 2017, 139, 2224−2233

5c), this phenomenon indicated that the coverage of Pt atoms should be optimized. The formation of bimetallic Ag−Pt nanocages can significantly enhance the electromagnetic field nearby as compared to a pure Pt nanocage. Forming Ag−Pt bimetallic system can facilitate effective adsorption/desorption of reactants with the presence of Ag atoms adjacent to active Pt atoms owing to the LSPR effects. This plasmon-induced electromagnetic field might be another factor to facilitate the suppression of peroxide yield through improving the efficient adsorption/desorption of reactants.

It is imperative to decouple the individual contribution from various plasmon-induced effects, various results including the limited current density enhancement (Δj), peroxide yield decrease, and relative vacancy decrease were plotted in Figure 11a. Apparently, a clearly volcanic tendency was observed that the AgPt-30 sample achieved the highest performance in limited current enhancement, suppression in peroxide yield and relative vacancy decrease among all samples. Most interestingly, the tendency of peroxide yield decrease seemed to be coincident with that of the relative vacancy decrease as a result of plasmon-induced hot electron transfer, revealed that suppression of peroxide yield could be mainly ascribed to the transfer of hot electron into Pt. In the case of AgPt-15 and AgPt-30 samples, the outermost surface have not been fully covered by Pt atoms from sequential formation, the hot electron transfer can remarkably affect the surface Pt atoms which significantly contact with nearby Ag atoms. Accompanying the decrease of Ag amount, newly formed Pt atoms grown onto the outermost surface of nanocages and further covered the most Ag-surrounded Pt atoms, leading to deficient transfers of hot electrons into Pt. These findings could also explicate that AgPt-45 and AgPt-60 samples failed to suppress the peroxide yield under light illumination owing to the absence of hot electron transfer into the outermost Pt even though the limiting currents were clearly improved. Accordingly, we can conclude that the formation of Ag−Pt bimetallic alloy with atomically physical contact is critical to perform this plasmon-induced peroxide suppression.

The hot electrons transfer from Ag to Pt might enhance the heterogeneity of surface charge and further facilitate the interaction between adsorbate and electrocatalyst while a similar case of Au−Pd nanostructure had reported,[46] this enhanced heterogeneity of surface charge would affect the adsorbing of oxygen gas (adsorbate). In addition, this plasmon-induced hot electron transfer also can result in a variation of electron distribution between adsorbate and electrocatalyst,[25] in which the plasmon-induced electron distribution that contained a higher population in those at or above the energy level of the antibonding orbital of adsorbate (i.e., O_2) was generated through hot electron transfer. As a consequence, plasmon-induced hot electron transfer processes could produce higher electron population in antibonding orbital of O_2 and weaken the bonding of O−O bond. This weakening of O−O bond can facilitate the bond breaking of O−O and leaving of desired H_2O, as plotted in Figure 11b. The absence of weakening effect might facilitate the bond breaking of O−Pt bond instead of O−O bond and lead to a formation of peroxide ions (HO_2^-). In this case, O_2 molecules weakly adsorbed onto the Pt surface, and the presence of Ag is essential to provide plasmon-induced effects for facilitating accommodation of O_2 on Pt atom surface. Notably, it has to be pointed out here that limiting current enhancement with a micro ampere scale is expectable, several reports have demonstrated the photocurrent density as a result of hot electron injection with an enhancement of μA−nA/cm^2 scale[23,47−49] that was similar to our finding with hundreds μA/cm^2 scale. As a result, despite the fact that both effects could significantly enhance the limiting current, we could conclude that the plasmon-induced hot electron transfer governed the suppression of peroxide formation instead of plasmon-induced heating that would only happen on outer surface of nanocage and cause a negative effect (i.e., increase in peroxide yield). The plasmon-induced electromagnetic field could facilitate the adsorbing and allow O_2 molecules to spend more time near the Pt surface, which made the populating upon O_2 antibonding orbital from hot electron transfer more efficient. This pronounced difference for limiting current and peroxide yield under chopped illumination offered an obvious signal that the behavior was driven by surface plasmon. Synergetic effect from LSPR effects in Ag−Pt bimetallic edgeless nanocages is present, where Pt atom acts as reactive sites with binding to oxygen and adjacent Ag atom makes the hot electron transfer into antibonding of oxygen more efficient.

CONCLUSIONS

In summary, Ag−Pt bimetallic nanocages with an edgeless feature have been demonstrated through a galvanic replacement reaction, and a custom-made RDE/RRDE working station was designed with the aim of in situ realizing the plasmon-induced effects toward the formation of peroxide intermediate. The edgeless Ag−Pt bimetallic nanocages with hollow interior performed newly plasmon-induced effects to suppress the formation of undesired peroxide intermediate. A photo-dependent property corresponding to LSPR in present nanostructure could evidently reveal that the plasmon-induced hot electron transfer governed the suppression of peroxide formation instead of plasmon-induced heating that would cause a negative effect (i.e., increase in peroxide yield), which could be attributed to the hot electron transfer that offered a sufficient energy to populate the antibonding orbital of O_2. We believe this synergetic strategy through plasmon-induced effects of bimetallic nanostructure can perform great potentials in various fields toward altering the chemical reactions.

ASSOCIATED CONTENT

Supporting Information

The Supporting Information is available free of charge on the ACS Publications website at DOI: 10.1021/jacs.6b09080.

Figures S1−S6 (PDF)

AUTHOR INFORMATION

Corresponding Author

*haomingchen@ntu.edu.tw

ORCID

Hao Ming Chen: 0000-0002-7480-9940

Notes

The authors declare no competing financial interest.

ACKNOWLEDGMENTS

We acknowledge support from the Ministry of Science and Technology, Taiwan (Contracts No. MOST 104-2113-M-213-001 and MOST 104-2113-M-002-011-MY2), and are grateful to Ms. Chia Ying Chien and Su Jen Ji of the Ministry of Science and Technology (National Taiwan University) for their assistance during SEM experiments and the support from Dr.

DOI: 10.1021/jacs.6b09080
J. Am. Chem. Soc. 2017, 139, 2224−2233

H. S. Sheu, Dr. Y. C. Chuang, Dr. Y. C. Lai and Mr. C. K. Chang for assistance at beamline 09A at the Taiwan Photon Source (TPS). We are also grateful to I-Huei Chen for TEM support. Technical support from NanoCore, the Core Facilities for Nanoscience and Nanotechnology at Academia Sinica in Taiwan, is acknowledged.

REFERENCES

(1) Katsounaros, I.; Cherevko, S.; Zeradjanin, A. R.; Mayrhofer, K. J. J. *Angew. Chem., Int. Ed.* **2014**, *53*, 102.
(2) Chen, C.; Kang, Y.; Huo, Z.; Zhu, Z.; Huang, W.; Xin, H. L.; Snyder, J. D.; Li, D.; Herron, J. A.; Mavrikakis, M.; Chi, M.; More, K. L.; Li, Y.; Markovic, N. M.; Somorjai, G. A.; Yang, P.; Stamenkovic, V. R. *Science* **2014**, *343*, 1339.
(3) Huang, X.; Zhao, Z.; Cao, L.; Chen, Y.; Zhu, E.; Lin, Z.; Li, M.; Yan, A.; Zettl, A.; Wang, Y. M.; Duan, X.; Mueller, T.; Huang, Y. *Science* **2015**, *348*, 1230.
(4) Zhang, L.; Roling, L. T.; Wang, X.; Vara, M.; Chi, M.; Liu, J.; Choi, S.-I.; Park, J.; Herron, J. A.; Xie, Z.; Mavrikakis, M.; Xia, Y. *Science* **2015**, *349*, 412.
(5) Holewinski, A.; Idrobo, J.-C.; Linic, S. *Nat. Chem.* **2014**, *6*, 828.
(6) Sun, X.; Li, D.; Ding, Y.; Zhu, W.; Guo, S.; Wang, Z. L.; Sun, S. *J. Am. Chem. Soc.* **2014**, *136*, 5745.
(7) Guo, S.; Zhang, X.; Zhu, W.; He, K.; Su, D.; Mendoza-Garcia, A.; Ho, S. F.; Lu, G.; Sun, S. *J. Am. Chem. Soc.* **2014**, *136*, 15026.
(8) Sanchez-Sanchez, C. M.; Solla-Gullon, J.; Vidal-Iglesias, F. J.; Aldaz, A.; Montiel, V.; Herrero, E. *J. Am. Chem. Soc.* **2010**, *132*, 5622.
(9) Tao, A. R.; Habas, S.; Yang, P. *Small* **2008**, *4*, 310.
(10) Halas, N. J.; Lal, S.; Chang, W. S.; Link, S.; Nordlander, P. *Chem. Rev.* **2011**, *111*, 3913.
(11) Dreaden, E. C.; Alkilany, A. M.; Huang, X. H.; Murphy, C. J.; El-Sayed, M. A. *Chem. Soc. Rev.* **2012**, *41*, 2740.
(12) Zuloaga, J.; Prodan, E.; Nordlander, P. *ACS Nano* **2010**, *4*, 5269.
(13) Oulton, R. F.; Sorger, V. J.; Zentgraf, T.; Ma, R.-M.; Gladden, C.; Dai, L.; Bartal, G.; Zhang, X. *Nature* **2009**, *461*, 629.
(14) Okamoto, K.; Niki, I.; Shvartser, A.; Narukawa, Y.; Mukai, T.; Scherer, A. *Nat. Mater.* **2004**, *3*, 601.
(15) Luk'yanchuk, B.; Zheludev, N. I.; Maier, S. A.; Halas, N. J.; Nordlander, P.; Giessen, H.; Chong, C. T. *Nat. Mater.* **2010**, *9*, 707.
(16) Kaelberer, T.; Fedotov, V. A.; Papasimakis, N.; Tsai, D. P.; Zheludev, N. I. *Science* **2010**, *330*, 1510.
(17) Stockman, M. *Phys. Rev. Lett.* **2004**, *93*, 137404.
(18) Maier, S. A.; Kik, P. G.; Atwater, H. A.; Meltzer, S.; Harel, E.; Koel, B. E.; Requicha, A. A. G. *Nat. Mater.* **2003**, *2*, 229.
(19) Kleijn, S. E. F.; Lai, S. C. S.; Koper, M. T. M.; Unwin, P. R. *Angew. Chem., Int. Ed.* **2014**, *53*, 3558.
(20) Ye, J.; Wen, F. F.; Sobhani, H.; Lassiter, J. B.; Van Dorpe, P.; Nordlander, P.; Halas, N. J. *Nano Lett.* **2012**, *12*, 1660.
(21) Gao, H.; Liu, C.; Jeong, H. E.; Yang, P. *ACS Nano* **2012**, *6*, 234.
(22) Chen, H. M.; Chen, C. K.; Chen, C.-J.; Cheng, L.-C.; Wu, P. C.; Cheng, B. H.; Ho, Y. Z.; Tseng, M. L.; Hsu, Y.-Y.; Chan, T.-S.; Lee, J.-F.; Liu, R.-S.; Tsai, D. P. *ACS Nano* **2012**, *6*, 7362.
(23) DuChene, J. S.; Sweeny, B. C.; Johnston-Peck, A. C.; Su, D.; Stach, E. A.; Wei, W. D. *Angew. Chem., Int. Ed.* **2014**, *53*, 7887.
(24) Brongersma, M. L.; Halas, N. J.; Nordlander, P. *Nat. Nanotechnol.* **2015**, *10*, 25.
(25) Linic, S.; Aslam, U.; Boerigter, C.; Morabito, M. *Nat. Mater.* **2015**, *14*, 567.
(26) Clavero, C. *Nat. Photonics* **2014**, *8*, 95.
(27) Huang, Y.-F.; Zhang, M.; Zhao, L.-B.; Feng, J.-M.; Wu, D.-Y.; Ren, B.; Tian, Z.-Q. *Angew. Chem., Int. Ed.* **2014**, *53*, 2353.
(28) Mukherjee, S.; Libisch, F.; Large, N.; Neumann, O.; Brown, L. V.; Cheng, J.; Lassiter, J. B.; Carter, E. A.; Nordlander, P.; Halas, N. J. *Nano Lett.* **2013**, *13*, 240.
(29) Cao, L.; Barsic, D. N.; Guichard, A. R.; Brongersma, M. L. *Nano Lett.* **2007**, *7*, 3523.
(30) Hirsch, L. R.; Stafford, R. J.; Bankson, J. A.; Sershen, S. R.; Rivera, B.; Price, R. E.; Hazle, J. D.; Halas, N. J.; West, J. L. *Proc. Natl. Acad. Sci. U. S. A.* **2003**, *100*, 13549.
(31) Sun, Y. G.; Xia, Y. N. *Science* **2002**, *298*, 2176.
(32) Tao, A.; Sinsermsuksakul, P.; Yang, P. *Nat. Nanotechnol.* **2007**, *2*, 435.
(33) Sun, Y.; Xia, Y. *J. Am. Chem. Soc.* **2004**, *126*, 3892.
(34) Sun, Y. G.; Xia, Y. N. *J. Am. Chem. Soc.* **2004**, *126*, 3892.
(35) Li, J.; Liu, J.; Yang, Y.; Qin, D. *J. Am. Chem. Soc.* **2015**, *137*, 7039.
(36) Bard, A. J.; Faulkner, L. R. *Electrochemical Methods: Fundamentals and Applications*; Wiley: New York, 2001.
(37) Lee, K.; Zhang, L.; Lui, H.; Hui, R.; Shi, Z.; Zhang, J. J. *Electrochim. Acta* **2009**, *54*, 4704.
(38) Zhao, X. J.; Zhao, H. Y.; Zhang, T. T.; Yan, X. C.; Yuan, Y.; Zhang, H. M.; Zhao, H. J.; Zhang, D. M.; Zhu, G. S.; Yao, X. D. *J. Mater. Chem. A* **2014**, *2*, 11666.
(39) Han, P.; Bartels, D. M. *J. Phys. Chem.* **1996**, *100*, 5597.
(40) Wang, X. M.; Orikasa, Y.; Takesue, Y.; Inoue, H.; Nakamura, M.; Minato, T.; Hoshi, N.; Uchimoto, Y. *J. Am. Chem. Soc.* **2013**, *135*, 5938.
(41) Chung, H. T.; Won, J. H.; Zelenay, P. *Nat. Commun.* **2013**, *4*, 1922.
(42) Hu, G. Z.; Nitze, F.; Gracia-Espino, E.; Ma, J. Y.; Barzegar, H. R.; Sharifi, T.; Jia, X. E.; Shchukarev, A.; Lu, L.; Ma, C. S.; Yang, G.; Wagberg, T. *Nat. Commun.* **2014**, *5*, 5253.
(43) Kuttiyiel, K. A.; Sasaki, K.; Su, D.; Wu, L. J.; Zhu, Y. M.; Adzic, R. R. *Nat. Commun.* **2014**, *5*, 5185.
(44) Richardson, H. H.; Carlson, M. T.; Tandler, P. J.; Hernandez, P.; Govorov, A. O. *Nano Lett.* **2009**, *9*, 1139.
(45) Chen, H. M.; Liu, R.-S.; Lo, M.-Y.; Chang, S.-C.; Tsai, L.-D.; Peng, Y.-M.; Lee, J.-F. *J. Phys. Chem. C* **2008**, *112*, 7522.
(46) Zheng, Z.; Tachikawa, T.; Majima, T. *J. Am. Chem. Soc.* **2015**, *137*, 948.
(47) Lee, Y. K.; Jung, C. H.; Park, J.; Seo, H.; Somorjai, G. A.; Park, J. Y. *Nano Lett.* **2011**, *11*, 4251.
(48) Liu, Z.; Hou, W.; Pavaskar, P.; Aykol, M.; Cronin, S. B. *Nano Lett.* **2011**, *11*, 1111.
(49) Thomann, I.; Pinaud, B. A.; Chen, Z.; Clemens, B. M.; Jaramillo, T. F.; Brongersma, M. L. *Nano Lett.* **2011**, *11*, 3440.

DOI: 10.1021/jacs.6b09080
J. Am. Chem. Soc. 2017, 139, 2224−2233